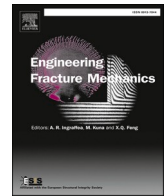




ELSEVIER

Contents lists available at ScienceDirect

# Engineering Fracture Mechanics

journal homepage: [www.elsevier.com/locate/engfracmech](http://www.elsevier.com/locate/engfracmech)

## Fracture analysis of hyperelastic membrane using bond-associated non-ordinary state-based peridynamics

Yang Yang<sup>a,\*</sup>, Yujie Chen<sup>b</sup>, Yijun Liu<sup>b</sup><sup>a</sup> Faculty of Material Science, Shenzhen MSU-BIT University, Shenzhen, Guangdong 518172, China<sup>b</sup> Department of Mechanics and Aerospace Engineering, Southern University of Science and Technology, Shenzhen, China

## ARTICLE INFO

## Keywords:

Hyperelastic membrane  
Large deformation  
Failure analysis  
Bond-associated non-ordinary state-based peridynamics  
Gent model

## ABSTRACT

In this paper, a non-ordinary state-based peridynamics model (NOSB PD) has been proposed to simulate the large deformation and failure analysis of hyperelastic membranes. To account for the curving horizon of the membrane, a non-local membrane theory has been developed by approximating it as a flat surface and applying the plane stress assumption locally. Thus, the membrane structure is simulated using a single layer of material points, which simplifies implementation, improves efficiency, and avoids volume locking. The Gent model has been employed to simulate the hyperelastic material constitutively, as it has an elegant mathematical framework and can achieve the entire range of stretches. Furthermore, Bond-associate NOSB PD is utilized to overcome zero-energy modes without affecting the material properties. A modification has been addressed to overcome the boundary effect by adding a complementary force density to the boundary nodes. The accuracy of large deformation and incompressibility of the developed models are verified by the corresponding finite element analyses. Finally, the proposed method is demonstrated by presenting some benchmark examples, and the results illustrate the accuracy and efficiency of the proposed method for the large deformation, fracture, and off-plane tearing analyses of hyperelastic membranes.

### 1. Introduction

Hyperelastic materials are substances that can undergo large deformation under relatively small stress. These materials are commonly found in nature, such as in biological tissues and spider silk. Man-made hyperelastic materials, such as rubbers and foams, have also been created and are widely used in various industries. With the advancements in material science and artificial intelligence robots, several new superelastic materials have been developed and applied in diverse fields, such as biomechanics and nanostructures in the form of membrane structures. However, the lower stiffness of membrane structures, which simultaneously involves material non-linearity from constitutive relations and geometrical non-linearity from kinematics, makes simulating fractures in hyperelastic membranes a significant challenge. Therefore, it is crucial to develop a novel membrane damage model.

Modeling the failure of material and structure is a challenge in the field of computational mechanics. Classical continuum mechanics, which is based on spatial derivatives, faces inherent difficulties in describing spatial discontinuity and singular stress fields around the crack. Peridynamics was proposed by Silling in 2000 [1]. This nonlocal continuum mathematical formulation is particularly useful in solving discontinuity problems, as the nonlocal integral form of the equations supplies a much larger function space for

\* Corresponding author.

E-mail address: [yangy2023@smbu.edu.cn](mailto:yangy2023@smbu.edu.cn) (Y. Yang).

<https://doi.org/10.1016/j.engfracmech.2024.110131>

Received 29 February 2024; Received in revised form 23 April 2024; Accepted 2 May 2024

Available online 3 May 2024

0013-7944/© 2024 Elsevier Ltd. All rights reserved.

the solutions. With PD, the failure initiation and propagation can be naturally captured and represented without additional artificial treatments. Therefore, PD has attracted significant research interest in modeling fracture [2–4].

The literature on PD modeling of hyperelastic membranes has been limited so far. One of the main challenges faced is the complicated constitutive model that arises from the material's complex composition. Silling and Bobaru [5] used a bond-based PD model to approximate the large deformation and failure behaviors of rubber membranes. This method employs a constitutive model of rubber material under a particular loading condition. However, due to the lack of bonds extending to particles off the surface, a given force density will result in different bulk material responses using the governing equation based on 3D expression. Bang and Madenci [6] presented the PD modeling of hyperelastic membrane deformation using the Neo-Hookean model to simulate material behavior. Equibiaxial, planar and uniaxial loading conditions were considered in the analyses. The material parameters for each loading case were determined by equating the PD strain energy density to that of the classical continuum mechanics. The results were compared well with finite element analysis. Li et al. [7] studied the quasi-static behaviors of membranes with an implicit bond-based PD computational framework. They developed a bimodular material model in PD, which was extended to deal with the wrinkling and fracture problems of membranes by setting the compressive micro-modulus to be zero. Besides, Oterkus et al. [8] presented a new PD shell membrane formulation. The equations of motion were obtained using the Euler-Lagrange equation, and the bond constant was determined by comparing PD and classical equations of motion for shell membranes for a particular condition of PD internal length parameter, horizon, approaching zero. Ozdemir et al. [9] developed a viscoelastic material model in the ordinary state-based PD framework to capture crack propagation in polymeric water treatment membranes. Yang et al. [10] derived an analytical solution of the PD equation of motion for a 2-D rectangular membrane.

Most of the above work relies on the bond-based PD model. However, BB PD has a significant drawback: Poisson's ratio is fixed at 1/3 for plane stress, and 1/4 for plain strain and 3D problems [11]. With some modifications, BB PD can involve plasticity and rate-dependent behaviors [12], and also can capture the large deformation of the hyperelastic under particular loading conditions. However, BBPD cannot accurately predict the bulk hyperelastic behavior of structures under most loading conditions. To overcome these limitations, state-based PD including ordinary state-based (OSB) PD [13] and non-ordinary state-based (NOSB) PD [14] was developed, which can merge various material models in the local realm.

NOSB PD uses a stress–strain relationship from the local theory to determine the interaction force between particles and bridge the gap between local and non-local material models [14]. It has been extended to simulate complex material models [3,4,15] and solve a variety of problems. However, conventional NOSB PD suffers from zero-energy modes, which can cause significant numerical oscillation due to a non-unique mapping between the deformation states and force states. To control the nonphysical oscillations and improve numerical results, many stabilization techniques have been developed, such as introducing a fictitious spring force to a bond [16], using the average displacement correction over a horizon [16] and applying higher-order deformation gradient tensor [17]. One of the most promising solutions to zero-energy modes is bond-associated (BA) non-ordinary state-based (NOSB) PD. It uses the points within a bond proximity to calculate the bond's deformation gradient, avoiding the zero-energy mode inherently without extra corrections or affecting the material characteristics [18–20]. Based on BA NOSB PD, the in-plane deformation and crack growth were analyzed in hyperelastic material of Neo-Hookean model [21], Anand model [22] and Gent model [2,3].

Membrane structures are very thin and lack bending stiffness. When using 3D meshing, fine discretization is required, leading to high computational expense. The PD method is generally more costly than the local method due to the non-local nature of PD modeling, which requires more interaction forces to be calculated. Although PD can be coupled with the finite element method [23,24] and boundary element method [25,26] to reduce the computational cost. It is essential to simplify the 3D PD model whenever possible. The mechanical properties of the membrane comply with the plane stress assumption, and hence, in this paper, a non-local membrane theory is developed based on the 2D plane stress assumption within the framework of NOSB PD. The membrane structure is simulated using a single layer of material points, simplifying implementation, improving efficiency, and avoiding volume locking. The Gent model is used to simulate the hyperelastic material constitutive as it has an elegant mathematical framework and can be applied over the entire range of stretches. Furthermore, the deformation gradient-based constitutive relation of the Gent model can be quickly introduced in the PD correspondence model with NOSB PD framework. BA NOSB PD is utilized to overcome zero-energy modes without affecting the material properties. The accuracy of large deformation and incompressibility of the developed models are verified by the corresponding finite element analyses. Some benchmark examples are presented and the results demonstrate the accuracy and efficiency of the proposed method for the large deformation, fracture and off-plane tearing analyses of hyperelastic membranes.

The remaining sections of this paper are organized as follows. Section 2 provides a brief review of the theory of NOSB PD. In section 3, a PD hyperelastic continuum membrane theory is developed. Section 4 describes the BA NOSB PD technique that is used to overcome the zero-model. Section 5 presents the verification and several numerical examples. Finally, the conclusions of this paper are discussed in Section 6.

## 2. Non-ordinary state-based PD theory

PD is based on non-local theory. The motion equation of a material point  $i$  is expressed in an integration from as:

$$\rho_i \ddot{\mathbf{u}}_i = \int_{H_i} [\mathbf{T}_i \langle \mathbf{X}_{ij} \rangle - \mathbf{T}_j \langle \mathbf{X}_{ji} \rangle] dV_j + \mathbf{b}_i \quad (1)$$

where  $\rho_i = \rho(\mathbf{X}_i)$ ,  $\ddot{\mathbf{u}}_i = \ddot{\mathbf{u}}(\mathbf{X}_i, t)$  and  $\mathbf{b}_i = \mathbf{b}(\mathbf{X}_i, t)$  are the mass density, acceleration and body force density vectors, respectively. The

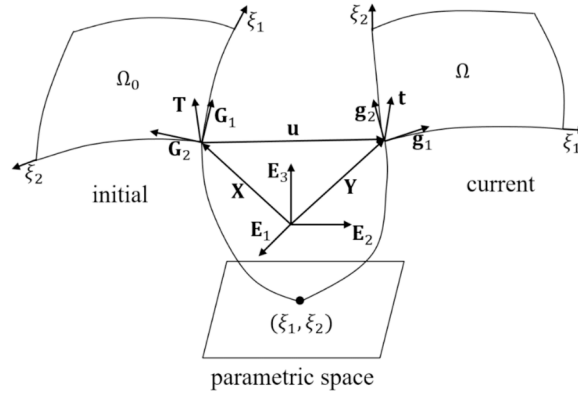


Fig. 1. Kinematic description of membrane.

initial position vector of material point  $i$  is represented  $X_i$ . The internal force at  $X_i$  is calculated in the PD form by summing up the interactions between  $X_i$  and  $X_j$  within the horizon  $H_i$ .  $H_i$  is a horizon of material point  $i$ , usually characterized by a circle centered on the material point  $i$  with a radius of  $\delta$ . The volume occupied by material point  $j$  in  $H_i$  is denoted by  $V_j$ . For convenience, the bond vector in the initial configuration is defined as  $X_{ij} = X_j - X_i$ . The internal force state of material point  $i$  is computed using the NOSB PD method in the form of:

$$T_i(X_{ij}) = w(|X_{ij}|)P_iK_i^{-1}X_{ij} \tag{2}$$

Tensor  $P$  is the first Piola-Kirchhoff stress tensor expressed as:

$$P = \frac{\partial \Psi}{\partial F} \tag{3}$$

in which  $\Psi$  is the strain energy density function. The deformation gradient tensor  $F$  is defined by:

$$F = \frac{\partial Y}{\partial X} \text{ and } F_i = \left[ \int_{H_i} w(|X_{ij}|)(Y_{ij} \otimes X_{ij})dV_j \right] K_i^{-1} \tag{4}$$

where  $Y$  is the position vector in the current configuration and  $Y_{ij}$  is the current bond vector.  $\otimes$  denotes the dyadic product of two vectors. The scalar-valued function  $w$  is the weight function evaluating the influence of different neighborhood points. Usually,  $w$  is the function of bond length  $|X_{ij}|$ . In this paper, the weight function takes the form:

$$w(|X_{ij}|) = 1 - \frac{|X_{ij}|}{\delta} \tag{5}$$

Tensor  $K$  is the shape tensor written as

$$K_i = \int_{H_i} w(|X_{ij}|)(X_{ij} \otimes X_{ij})dV_j \tag{6}$$

Besides, one may deduce or define a non-local differential operator similar as Eq. (4) (see Ref. [27,28]) as

$$\nabla_x \otimes f|_{x_i} = \left[ \int_{H_i} w(|X_{ij}|)(f_{ij} \otimes X_{ij})dV_j \right] \cdot K_i^{-1} \tag{7}$$

### 3. A PD hyperelastic continuum membrane theory

The non-local membrane theory is based on the idea of approximating a curving horizon as a flat surface. This allows for the application of the plane stress assumption locally. In section 3.1, the kinematics of membrane structure is presented. This framework is established based on the shell theory developed in Ref. [29]. Section 3.2 offers the local constitutive relation of the Gent model under plane stress assumption. Finally, section 3.3 presents the non-local balance law of linear momentum for the membrane.

#### 3.1. Kinematics

The following is a kinematic explanation of the curved membrane as shown in Fig. 1. The initial and deformed configurations are represented by mid-surface  $\Omega_0$  and  $\Omega$  respectively. The membrane is modeled as a single layer of material points. Each point has three

degrees of freedom in translation.

First, a compact parametric space  $\mathbf{A} \subset \mathbb{R}^2$  with boundary  $\partial\mathbf{A}$  is defined. Points in the parametric space denoted by  $\xi \in \mathbf{A}$ :

$$\xi = \xi_1 \mathbf{E}_1 + \xi_2 \mathbf{E}_2 \tag{8}$$

The position vector of a material point at a distance  $\eta$  from the mid-surface in the initial configuration can be expressed as

$$\mathbf{X} = \Phi^0(\xi_1, \xi_2, \eta) = \boldsymbol{\varphi}^0 + \eta \mathbf{D}(\xi_1, \xi_2), (\xi_1, \xi_2) \in \mathbf{A} \text{ and } \eta \in \left[-\frac{h}{2}, \frac{h}{2}\right] \tag{9}$$

where  $\boldsymbol{\varphi}^0$  defines the in-plane position of the membrane.  $\eta$  presents the thickness coordinate and  $h$  is the membrane thickness. Vector  $\mathbf{D}$  is the pseudo normal vector of the membrane in the initial configuration with  $|\mathbf{D}| = 1$ . The convected basis vector  $\mathbf{G}$  in the initial configuration is defined as the derivatives of  $\Phi^0$  with respect to coordinates  $\xi_\alpha$ :

$$\mathbf{G}_\alpha = \boldsymbol{\varphi}^0(\xi_1, \xi_2)_{,\alpha} + \eta \mathbf{D}_{,\alpha}, \alpha = 1, 2 \text{ and } \mathbf{G}_3 = \mathbf{D} \tag{10}$$

In this work, an appropriate selection  $\xi_\alpha$  to make  $\mathbf{G}_1$ ,  $\mathbf{G}_2$  and  $\mathbf{G}_3$  mutually perpendicular, forming an orthogonal local vector basis.

Similarly, the position vector in the current configuration can be written as

$$\mathbf{Y} = \Phi(\xi_1, \xi_2, \eta) = \boldsymbol{\varphi}(\xi_1, \xi_2) + \eta \mathbf{d}(\xi_1, \xi_2), (\xi_1, \xi_2) \in \mathbf{A} \text{ and } \eta \in \left[-\frac{h}{2}, \frac{h}{2}\right] \tag{11}$$

And the corresponding convected vectors are obtained by

$$\mathbf{g}_\alpha = \boldsymbol{\varphi}(\xi_1, \xi_2)_{,\alpha} + \eta \mathbf{d}_{,\alpha}, \alpha = 1, 2 \text{ and } \mathbf{g}_3 = \mathbf{d} \tag{12}$$

Here, neglecting the shear deformation along the thickness of membrane,  $\mathbf{g}_3$  is still perpendicular to  $\mathbf{g}_1$  and  $\mathbf{g}_2$ . That is

$$\mathbf{g}_3 = \frac{\partial \mathbf{Y}}{\partial \eta} = \frac{\mathbf{g}_1 \times \mathbf{g}_2}{|\mathbf{g}_1 \times \mathbf{g}_2|} = \mathbf{d} \tag{13}$$

### 3.2. The deformation gradient

In the framework of NOSB PD, deformation gradient is a crucial factor needs to be determined first. For a given motion  $\Phi$ , its deformation in terms of the convective coordinates can be obtained via the Fréchet derivative [29], which is denoted by  $\nabla \Phi$  related to the parametric configuration  $\{\mathbf{E}_I\}_{I=1,2,3}$  (with  $\xi_3 = \eta$ ),

$$\nabla_\xi \Phi = \frac{\partial \Phi}{\partial \xi_I} \otimes \mathbf{E}_I \equiv \mathbf{g}_I \otimes \mathbf{E}_I \tag{14}$$

where  $\mathbf{E}_I$  is an orthonormal basis. Then, the deformation gradient can be expressed using the chain rule

$$\mathbf{F} = \frac{\partial \mathbf{Y}}{\partial \mathbf{X}} = \nabla_\xi \Phi \cdot (\nabla_\xi \Phi^0)^{-1} \tag{15}$$

Note that

$$\nabla_\xi \Phi^0 = \nabla_\alpha \Phi^0 + \mathbf{D} \otimes \mathbf{E}_3 = \boldsymbol{\varphi}^0_{,\alpha} \otimes \mathbf{E}_\alpha + \mathbf{D} \otimes \mathbf{E}_3, \alpha = 1, 2 \tag{16}$$

$$\nabla_\xi \Phi = \nabla_\alpha \Phi + \mathbf{d} \otimes \mathbf{E}_3 = \boldsymbol{\varphi}_{,\alpha} \otimes \mathbf{E}_\alpha + \mathbf{d} \otimes \mathbf{E}_3, \alpha = 1, 2 \tag{17}$$

where  $\nabla_\xi \Phi$  denotes the gradient on the tangent space at node  $\Phi$ , and

$$\nabla_\alpha = \frac{\partial}{\partial \xi_\alpha} \mathbf{E}_\alpha, \alpha = 1, 2 \tag{18}$$

According to Eq. (7), the derivatives of the initial position vector on the mid-surface with respect to  $\xi_\alpha$  at material point  $i$  can be expressed as

$$\boldsymbol{\varphi}^0_{,\alpha}|_i = \left[ \int_{H_i} w(|\xi_{ij}|) (\boldsymbol{\varphi}^0_{ij} \otimes \xi_{ij}) dS_j \right] \cdot \mathbf{K}_i^{-1} \tag{19}$$

where

$$\mathbf{K}_i = \int_{H_i} w(|\xi_{ij}|) \cdot (\xi_{ij} \otimes \xi_{ij}) dS_j \tag{20}$$

Here, it is worth noting that  $\varphi_{,\alpha}^0$  is a 3-by-2 matrix and  $\mathbf{K}$  is a 2-by-2 matrix. Similarly, the derivatives of the current position vector on the mid-surface with respect to  $\xi_\alpha$  can be expressed as

$$\varphi_{,a}|_i = \left[ \int_{H_i} w(|\xi_{ij}|)(\varphi_{ij} \otimes \xi_{ij}) dS_j \right] \cdot \mathbf{K}_i^{-1} \quad (21)$$

Then,  $\nabla_\xi \Phi^0$  can be written in a matrix form as

$$\nabla_\xi \Phi^0 = \begin{bmatrix} \frac{\partial \varphi_1^0}{\partial \xi_1} & \frac{\partial \varphi_1^0}{\partial \xi_2} & D_1 \\ \frac{\partial \varphi_2^0}{\partial \xi_1} & \frac{\partial \varphi_2^0}{\partial \xi_2} & D_2 \\ \frac{\partial \varphi_3^0}{\partial \xi_1} & \frac{\partial \varphi_3^0}{\partial \xi_2} & D_3 \end{bmatrix} = [\mathbf{G}_1 \quad \mathbf{G}_2 \quad \mathbf{D}] \quad (22)$$

And  $\nabla_\xi \Phi$  can be written as

$$\nabla_\xi \Phi = \begin{bmatrix} \frac{\partial \varphi_1}{\partial \xi_1} & \frac{\partial \varphi_1}{\partial \xi_2} & d_1 \\ \frac{\partial \varphi_2}{\partial \xi_1} & \frac{\partial \varphi_2}{\partial \xi_2} & d_2 \\ \frac{\partial \varphi_3}{\partial \xi_1} & \frac{\partial \varphi_3}{\partial \xi_2} & d_3 \end{bmatrix} = [\mathbf{g}_1 \quad \mathbf{g}_2 \quad \mathbf{d}] \quad (23)$$

When the initial configuration is flat, then  $\xi_I = X_I$  and  $G_I = E_I$ , such that  $\nabla_\xi \Phi^0$  becomes an identity matrix. In following samples, the initial configuration is always flat.

Since the plane stress assumption is introduced locally to the membrane structure, the deformation gradient tensor must be converted to the local system using a rotation matrix  $\mathbf{Q}$

$$\mathbf{F}_{local} = \mathbf{Q}\mathbf{F} \quad (24)$$

where  $\mathbf{Q}$  can be constructed based on the convected basis vectors as

$$\mathbf{Q}^T = \begin{bmatrix} \frac{\mathbf{g}_1}{|\mathbf{g}_1|} & \frac{\mathbf{d} \times \mathbf{g}_1}{|\mathbf{d} \times \mathbf{g}_1|} & \mathbf{d} \end{bmatrix} \quad (25)$$

Other forms are possible for constructing  $\mathbf{Q}^T$ . The third column  $\mathbf{d}$ , represents the normal vector of the membrane and is perpendicular to the other columns. Then  $\mathbf{F}_{local}$  can be represented by a 2-by-2 matrix.

### 3.3. Constitutive relation

The Gent model is a great choice for capturing the hardening response of hyperelastic materials under large tensile stretch and is both elegant in expression. So, it has been selected as the constitutive model for this paper. Only a parameter  $J_m$  representing tensile limit needs to calibrate, in addition to the shear modulus and a bulk parameter  $D$ . The strain energy density can be expressed as

$$\Psi = -\frac{\mu J_m}{2} \ln\left(1 - \frac{\bar{I}_1 - 3}{J_m}\right) + \frac{1}{D} \left(\frac{J^2 - 1}{2} - \ln J\right) \quad (26)$$

where  $\bar{I}_1$  is the normalized first invariant of right Cauchy-Green strain tensor which can be expressed as  $\bar{I}_1 = \text{tr} \mathbf{C} J^{-2/3}$  with  $\mathbf{C} = \mathbf{F}^T \mathbf{F}$  and  $J = \det \mathbf{F}$ . The second term on the right-hand side represents the effect of volume change. For material with slight compressibility,  $D$  can be set to a relatively small value. Specially, if  $J_m$  tends to infinite, the expression of strain energy density is equivalent with the Neo-Hookean model.

The expression of the first Piola-Kirchhoff stress tensor of Gent model under plane stress assumption as derived in Ref. [3] takes the form:

$$\mathbf{P} = \mathbf{F}\mathbf{S} = \frac{\mu J^{-2/3} J_m}{J_m - \text{tr} \mathbf{C} J^{-2/3} + 3} (\mathbf{F} - C_{33} \mathbf{F}^{-T}) \quad (27)$$

For the numerical implementation in the case of plane stress,  $\text{tr} \mathbf{C}$  and  $J$  are expressed as follows, respectively

$$\begin{aligned} \text{tr} \mathbf{C} &= \text{tr} \tilde{\mathbf{C}} + C_{33} \\ J &= \sqrt{C_{33} J} \end{aligned} \quad (28)$$

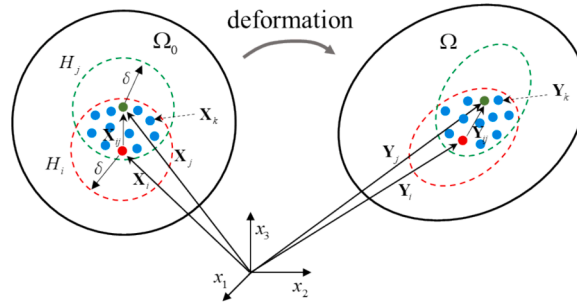


Fig. 2. Illustration of bond-associated scheme.

in which,  $tr\tilde{C} = C_{11} + C_{22}$  and  $\tilde{J} = \sqrt{C_{11}C_{22} - C_{12}^2}$ . The superscript “~” represents the tensor for 2D case. Then the stress tensor  $\mathbf{P}$  in 2D form is rewritten as

$$\tilde{\mathbf{P}} = \frac{\mu\tilde{J}^{-2/3}J_mC_{33}^{-1/3}}{J_m - (tr\tilde{C} + C_{33})\tilde{J}^{-2/3}C_{33}^{-1/3} + 3}(\tilde{\mathbf{F}} - C_{33}\tilde{\mathbf{F}}^{-T}) \quad (29)$$

$\tilde{\mathbf{F}}$  as the in-plane local deformation gradient tensor. And  $C_{33}$  can be calculated numerically from the equation

$$\frac{\mu\tilde{J}^{-2/3}J_mC_{33}^{-1/3}}{J_m - (tr\tilde{C} + C_{33})\tilde{J}^{-2/3}C_{33}^{-1/3} + 3}(\frac{2}{3}C_{33} - \frac{1}{3}tr\tilde{C}) + \frac{1}{D}(C_{33}J^2 - 1) = 0 \quad (30)$$

At this point, to obtain the first Piola-Kirchoff stress tensor in global system, the 2-by-2 tensor  $\tilde{\mathbf{P}}$  is first expanded to 3-by-3 tensor  $\mathbf{P}_{local}$  by adding extra zero terms. Then the rotation matrix is applied to obtain the global stress tensor:

$$\mathbf{P} = \mathbf{Q}^T \mathbf{P}_{local} \mathbf{Q} \quad (31)$$

### 3.4. Non-local balance law of linear momentum

Zhang et al. [29] derived the balance laws and nonlocal governing equations for Peridynamic shells using the element perspective. These equations are applicable to PD membrane structure as well. The governing equation for the linear momentum of the membrane in non-local form at the mean plane is as:

$$\rho_0 h \ddot{\varphi}_i = \int_{H_i} [\bar{T}_i \langle \xi_{ij} \rangle - \bar{T}_j \langle \xi_{ji} \rangle] dS_j + \bar{b}_i \quad (32)$$

where  $\bar{b}$  is the integral of the body force over the thickness expressed as

$$\bar{b} = \int_{-h/2}^{h/2} J_0 \mathbf{b} d\eta, J_0 = \det(\mathbf{F}_{\Phi^0}) \quad (33)$$

And  $\bar{T}$  is the force density vector defined on the mid-surface expressed as

$$\bar{T}_i \langle \xi_{ij} \rangle = w(|\xi_{ij}|) \Psi_i \mathbf{K}_i^{-1} \xi_{ij} \quad (34)$$

where is the stress resultant expressed as

$$\Psi = \int_{-h/2}^{h/2} \hat{\mathbf{P}}^0 d\eta, \text{ and } \hat{\mathbf{P}}^0 = \begin{bmatrix} \hat{P}_{11} & \hat{P}_{12} \\ \hat{P}_{21} & \hat{P}_{22} \\ \hat{P}_{31} & \hat{P}_{32} \end{bmatrix} \quad (35)$$

where  $\hat{\mathbf{P}} = J_0 \mathbf{P} \cdot (\mathbf{F}_{\Phi^0})^{-1}$  and  $\mathbf{P}$  in the first Piola-Kirchoff stress tensor in Eq. (31).

## 4. Bond-associated non-ordinary state-Based PD theory

Several of the equations above are based on the PD expression of deformation gradient tensor. However, it has been observed that the zero energy modes in NOSB PD may arise due to the non-unique mapping from the displacement state to the deformation gradient tensor [30]. To address this issue, the bond-associated scheme was proposed [31]. In the BA scheme, there is no extra compensation term or empirical parameter in the expression of force state, and the material properties remain unaffected.

As shown in Fig. 2, the expression of the deformation gradient is associated with a bond, and calculated using displacement information from the material points in the joint horizon of the bond end points, expressed as

$$\mathbf{F}_i \langle \mathbf{X}_{ij} \rangle = \left[ \int_{H_i \cap H_j} w(|\mathbf{X}_{ik}|) \mathbf{Y}_{ik} \otimes \mathbf{X}_{ik} dV_k \right] \cdot \mathbf{K}_i^{-1} \langle \mathbf{X}_{ij} \rangle \quad (36)$$

with the corresponding shape tensor written as

$$\mathbf{K}_i \langle \mathbf{X}_{ij} \rangle = \int_{H_i \cap H_j} w(|\mathbf{X}_{ik}|) \mathbf{X}_{ik} \otimes \mathbf{X}_{ik} dV_k \quad (37)$$

The force density vector is rewritten as

$$\mathbf{T}_i \langle \mathbf{X}_{ij} \rangle = \frac{1}{2} \frac{\phi_1 \langle \mathbf{X}_{ij} \rangle}{\phi_2 \langle \mathbf{X}_{ij} \rangle} w(|\mathbf{X}_{ij}|) \mathbf{P}_i \mathbf{K}_i \langle \mathbf{X}_{ij} \rangle \mathbf{X}_{ij} \quad (38)$$

where

$$\begin{aligned} \phi_1 \langle \mathbf{X}_{ij} \rangle &= \frac{\int_{H_i \cap H_j} dV_k}{\int_{H_i} dV_k} \\ \phi_2 \langle \mathbf{X}_{ij} \rangle &= \frac{\int_{H_i} dV_k}{\int_{H_i} dV_k + \int_{H_j} dV_k} \end{aligned} \quad (39)$$

In the same manner, Eq. (19) and (21) are rehearsed as

$$\varphi_{,a}^0 \langle \xi_{ij} \rangle |_{i} = \left[ \int_{H_i \cap H_j} w(|\xi_{ik}|) (\varphi_{ik}^0 \otimes \xi_{ik}) dS_k \right] \cdot \mathbf{K}_i^{-1} \langle \xi_{ij} \rangle \quad (40)$$

$$\varphi_{,a} \langle \xi_{ij} \rangle |_{i} = \left[ \int_{H_i \cap H_j} w(|\xi_{ik}|) (\varphi_{ik} \otimes \xi_{ik}) dS_k \right] \cdot \mathbf{K}_i^{-1} \langle \xi_{ij} \rangle \quad (41)$$

with the corresponding shape tensor written as

$$\mathbf{K}_i \langle \xi_{ij} \rangle = \int_{H_i \cap H_j} w(|\xi_{ik}|) (\xi_{ik} \otimes \xi_{ik}) dS_k \quad (42)$$

The expression for the force density vector, as given in Eq. (34), can be expressed as follows

$$\bar{\mathbf{T}}_i \langle \xi_{ij} \rangle = \frac{1}{2} \frac{\phi_1 \langle \xi_{ij} \rangle}{\phi_2 \langle \xi_{ij} \rangle} w(|\xi_{ij}|) \Psi_i \mathbf{K}_i^{-1} \langle \xi_{ij} \rangle \xi_{ij} \quad (43)$$

## 5. Computer implementation

### 5.1. Quasi-static

In the present work, a numerical damping term  $c$  is introduced in the kinematic equation to implement the governing equation in quasi-static solutions

$$\rho_i \ddot{\mathbf{u}}_i = \int_{H_i} [\mathbf{T}_i \langle \mathbf{X}_{ij} \rangle - \mathbf{T}_j \langle \mathbf{X}_{ji} \rangle] dV_i + \mathbf{b}_i - c \dot{\mathbf{u}}_i \quad (44)$$

The iteration is done in explicit form using the central difference scheme to achieve the temporal difference.

### 5.2. Boundary effects

According to the non-local theory, during implementation, the material near the boundary is chunked by the boundary of the geometry, resulting in an incomplete horizon. This leads to a significant boundary effect under 3D loading condition. To address this issue, a modification has been proposed. It involves adding a complementary force density to the boundary nodes. The complementary force density vector is perpendicular to the local plane, with the in-plane force state remaining unchanged. Thus, the state of plane stress is still valid. The complementary force density vector is expressed in the following format:

$$\mathbf{T}_i^c \langle \xi_{ij} \rangle = w(|\xi_{ij}|) \cdot \mathbf{A} \cdot \text{dot}(\mathbf{Y}_{ij}, \mathbf{d}_i) \cdot \text{direc}(\mathbf{Y}_{ij}) \quad (45)$$

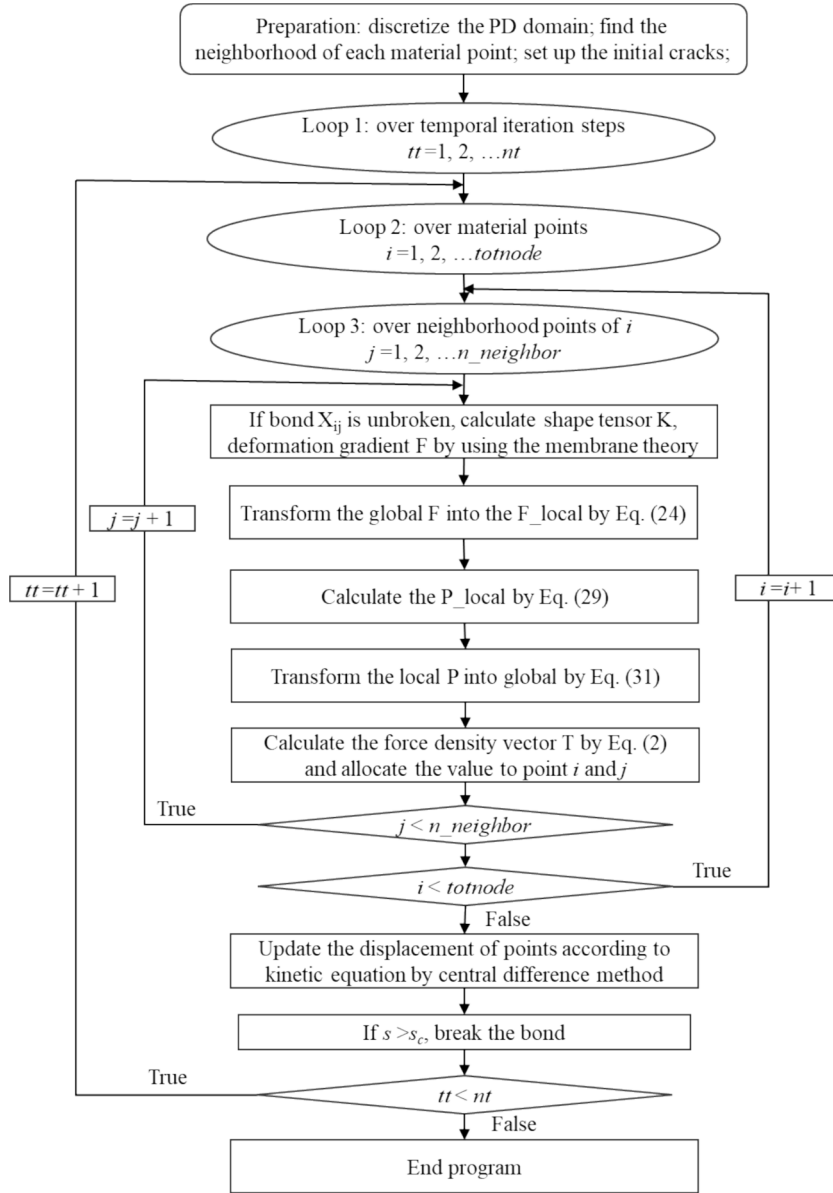


Fig. 3. Flowchart of the implementation process.

where parameter  $A$  is an empirical parameter,  $\langle \cdot \rangle$  is the term of dot product. Dot  $(Y_{ij}, d_i)$  means the projection of the current relative position on the normal direction of the local plane. The vector  $\text{direc}(Y_{ij}) = Y_{ij}/|Y_{ij}|$  is a unit vector.

### 5.3. Damage prediction

The modeling of crack in a PD framework is just removing the interaction of the bonds that pass across the crack. The failure criterion of a PD bond can base on the stretch of the bond  $s$ , which is defined as the ratio of the current bond length to the initial bond length:

$$s(X_{ij}, Y_{ij}) = \frac{|Y_{ij}|}{|X_{ij}|} \quad (46)$$

The effective stretch criterion, as defined in [32], is one of the failure criteria for hyperelastic material. It specifies a critical stretch  $s_c$  for a PD bond. If the stretch of a bond exceeds the critical stretch, the bond will break irreversibly. To record the failure of a bond, the force density vector is modified with a history-dependent function as

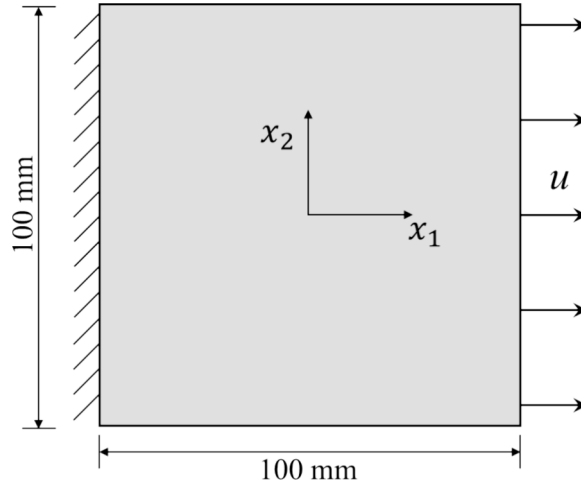


Fig. 4. Geometry and boundary conditions of a sheet under tension.

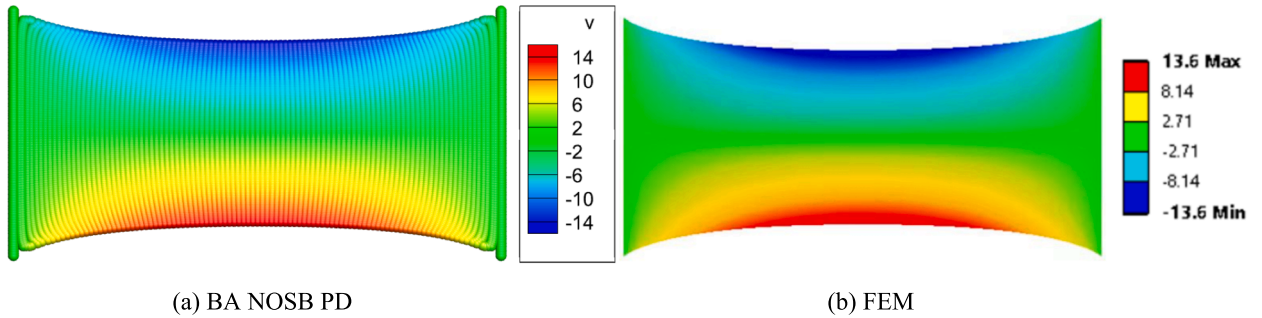


Fig. 5. Contour plot of longitudinal displacement. The unit is a millimeter.

$$T_i^* \langle X_{ij} \rangle = \gamma(s, t) T_i \langle X_{ij} \rangle \tag{47}$$

and

$$\gamma(s, t) = \begin{cases} 1, & \text{if } s(t') < s_c \text{ for all } 0 \leq t' \leq t \\ 0, & \text{otherwise} \end{cases} \tag{48}$$

The damage of a material point is defined as

$$dmg(X_i) = 1 - \frac{\int_{H_i} \gamma \langle X_{ij} \rangle dV_j}{\int_{H_i} dV_j} \tag{49}$$

The implementation process of this method is described by the following flowchart in Fig. 3.

### 6. Numerical examples

In this section, several typical examples are performed to validate the developed PD membrane model. The convergence behavior has been verified with respect to PD grid. The shear modulus is 1 kPa with  $1/D = 100$  kPa, and the stretch limit  $J_m$  is set at 160. These parameters are the same for all the following examples. The horizon radius is always set to  $\delta = 3.15 dx$ .

#### 6.1. Tension of a sheet

The dimensions of the sheet are stated as 100 mm in length, 100 mm in width and 1 mm in thickness, as illustrated in Fig. 3. The left edge of the sheet is fixed, and a displacement of  $u = 100$  mm is applied at the right edge. The model is discretized with spatial intervals.

To guarantee the convergence of the results, the plate is discretized along the width and height using 200 and 400 points, respectively. As a result of slight compressibility, there is significant vertical shrinkage. The predicted contour of the longitudinal

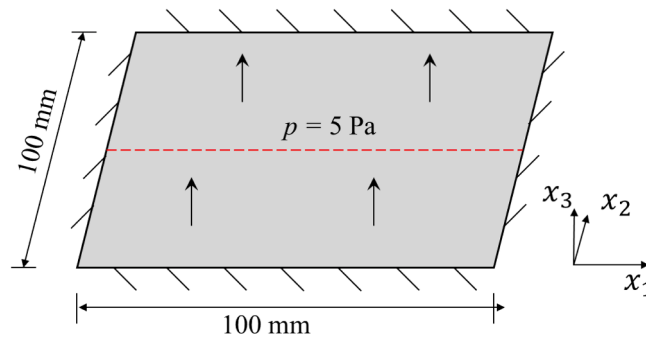


Fig. 6. Geometry and boundary conditions of a sheet under normal pressure.

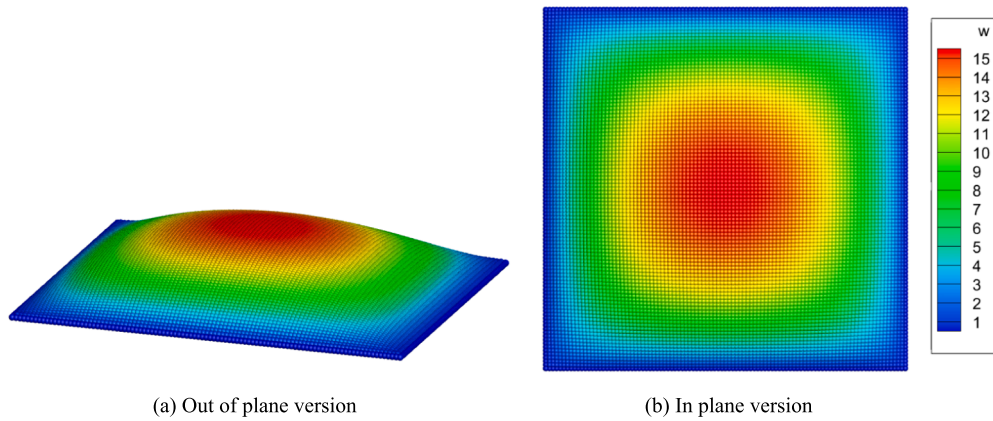


Fig. 7. Contour plot of vertical displacement. The unit is a millimeter.

displacement, denoted by  $v$ , is shown in Fig. 4. For comparison, the same example was analyzed by finite element method (FEM) with 2500 quadratic quadrilateral elements. The maximum longitudinal displacement occurs at the center of the bottom edge, measuring 14.06 mm in PD prediction and 13.57 mm in finite element analysis (FEA). The relative error between the two methods is 3.60 %. The primary source of the error in PD modeling is the boundary effect, meaning that the material properties at the edges and corners are less accurate than the bulk.

### 6.2. Rectangular sheet under normal pressure

The dimensions and sheet size of this example are identical to the previous one: 100 mm × 100 mm × 1 mm. A uniform pressure of 5 Pa is applied perpendicular to the deformed surface, as shown in Fig. 5. The four edges of the sheet are fixed. The spatial interval  $dx = 1$  mm.

In the deformed configuration, the vertical (out-plane) displacement is denoted as  $w$ . A plot (Fig. 6) is created to represent the distribution of  $w$ . The same example was analyzed using FEM with 10,000 elements. A comparison between the vertical displacement on the central horizontal line (the red line in Fig. 5) predicted by FEM and PD is plotted in Fig. 7. The maximum vertical displacement is found at the central point of the sheet, which is predicted to be 16.19 mm and 15.62 mm by PD and FEA respectively. The relative error between the two predictions is 3.60 %.

### 6.3. In-plane tension of a sheet with double-edge notches

As shown in Fig. 8, this example is a rectangular sheet with dimensions of 20 mm × 10 mm × 1 mm. Two pre-existing notches are located in the middle of the left and right edges. A velocity of 1.2 mm/s is applied to the top and bottom edges. The mass density of the sheet is 1000 kg/m<sup>3</sup>. The domain is discretized into 60 × 30 material points. In this numerical sample, the failure behavior is considered, and the critical stretch is set to 2.0.

The failure progression of this sample is plotted in Fig. 9. The Mode I crack extended horizontally until the sheet fractured into two pieces.

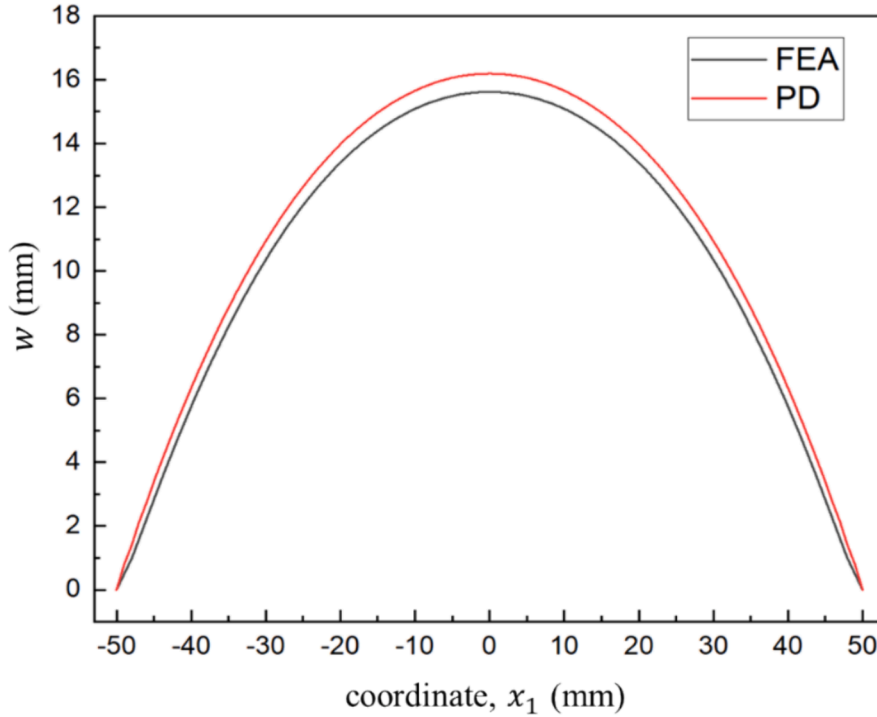


Fig. 8. Vertical displacement predicted by PD and FEA.

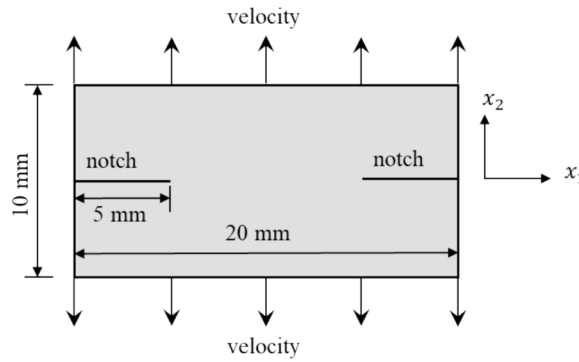


Fig. 9. Geometry and boundary conditions of a sheet under in-plane tension with two notches.

#### 6.4. Off-plane loading

In this section, the off-plane loading of a sheet is performed. The developed boundary effect modification is introduced on the free edge to improve numerical stability. The modification is also applied to the crack edges in the following example. The modification has little impact on the material properties.

A rectangular sheet with dimensions of 100 mm × 100 mm and a thickness of 1 mm is being considered, as shown in Fig. 10(a). The domain is discretized into 81 × 81 material nodes. The mass density is 1000 kg/m<sup>3</sup>. The left and right edges move in opposite directions out of the plane. As shown in Fig. 10(b), the loading velocity is 1 mm/s, which causes a vertical displacement, denoted as  $w$ . After 50 s, the location of the two edges remains constant.

As illustrated in Fig. 11, some nodes at the corners are located away from the local plane during the iteration processes. This is physically irrational and can lead to numerical instability. The reason for this can be attributed to the softening of the nodes due to the boundary effect. This effect causes less interaction forces, attracting the nodes to the local plane. To address this issue, modifications were made to the boundary effect, which resulted in several simulation steps shown in Fig. 12. It's important to note that the kinematic iteration would still converge with a smaller interval without the modification. The modification was necessary to solve the problem of the irrational location of the corner nodes under the boundary effect. It was also meant to allow for a larger temporal interval. This can be seen as introducing extra bending stiffness on the boundary. However, the overall material properties remain almost unchanged

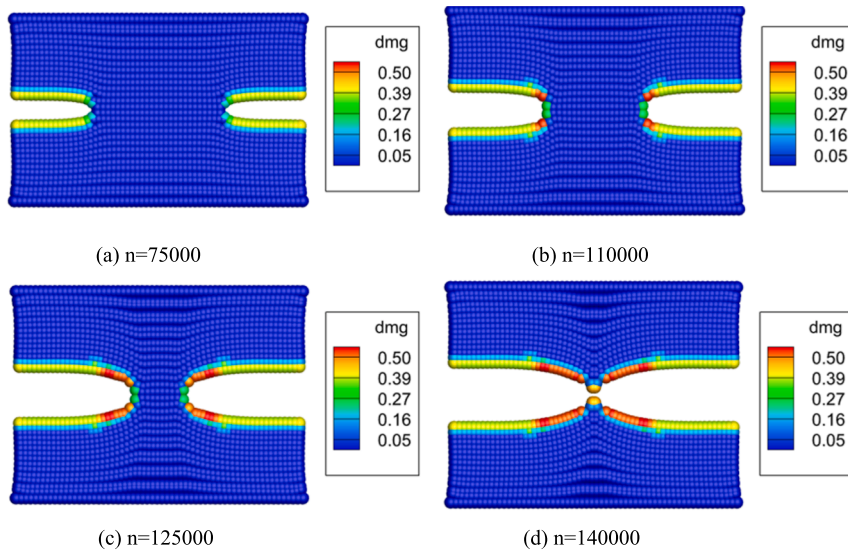


Fig. 10. Damage states of the sheet with double-edge notches.

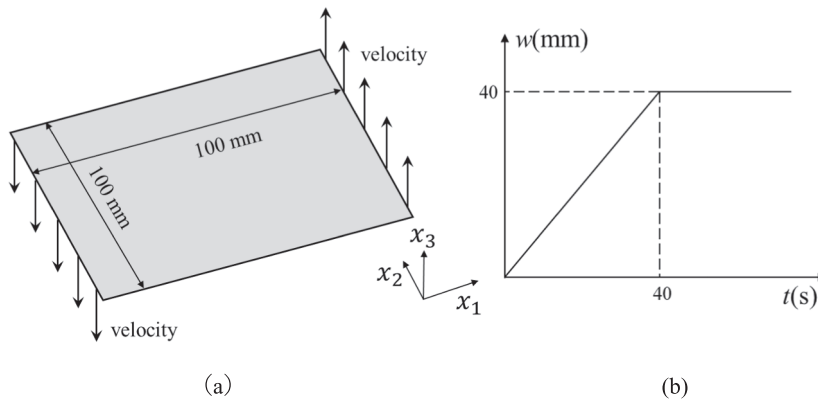


Fig. 11. Geometry and boundary conditions of a sheet under off-plane loading.

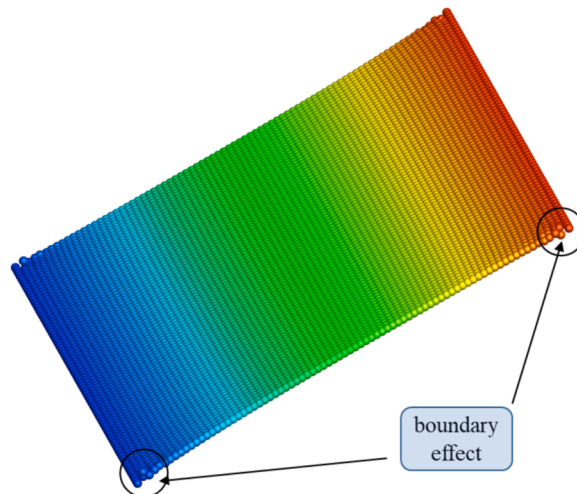


Fig. 12. Illustration of boundary effect.

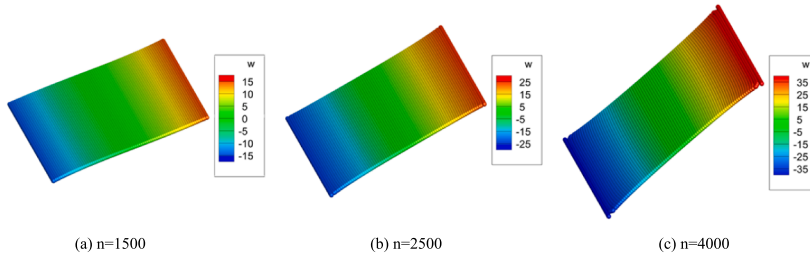


Fig. 13. Simulation of the sheet under off-plane loading.

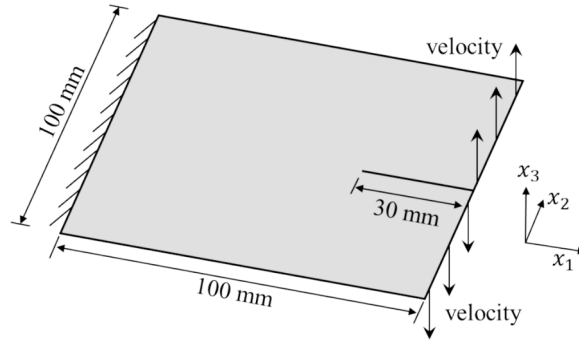


Fig. 14. Geometry and boundary conditions of a sheet under off-plane tear.

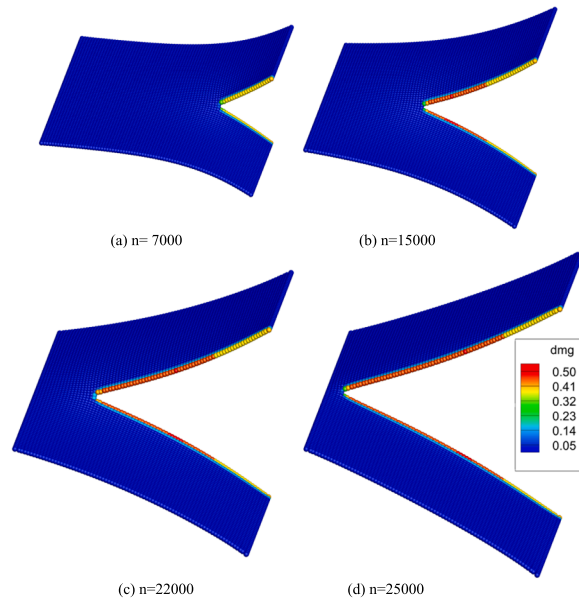


Fig. 15. Progressive damage of the sheet.

since the parameter  $A$  can be very small, and the modification was made only on a few material points. Fig. 13..

### 6.5. Off-plane tear

This example involves a rectangular sheet measuring with  $100\text{ mm} \times 100\text{ mm} \times 1\text{ mm}$ . The left side of the sheet is fixed. There is a pre-cut of  $30\text{ mm}$  on the middle of the right side. The two parts of the edges on the right side are subjected to velocity loading along  $x_3$  axis in opposite directions. The applied velocity is  $0.4\text{ mm/s}$ . The mass density is set at  $1000\text{ kg/m}^3$ . The domain is discretized into  $80 \times 80$  material points. For this example, the critical stretch is set to  $2.0$ .

The plotted progressive damages of the sheet are presented in Fig. 14. The crack propagates straight forward for some distance, corresponding with the experimental observation. Therefore, the proposed model is validated to describe the failure behavior effectively. Fig. 15.

## 7. Conclusions

A new model of non-ordinary peridynamics has been proposed in this paper to analyze the large deformation and failure behaviors of the hyperelastic membranes. By using the developed membrane theory, the membrane structures are simulated by a single layer of material points, which simplifies the implementation, improves the efficiency, and avoids the volume locking. The hyperelastic characteristics of the membrane are achieved by employing the Gent model with an elegant mathematic framework and the ability to capture the entire range of stretches. The bond-associated technique is applied to overcome the zero-energy modes without affecting the material properties. However, calculating the deformation gradient from material points to bonds also decreases efficiency. A modification by adding a complementary force density to the boundary nodes has been addressed to overcome the boundary effect. The large deformation and shrinkage results of the developed model are compared well to those of finite element analyses, and the efficiency of the present method is even better. Several benchmark numerical examples demonstrate that the developed model is accurate and efficient in analyzing the hyperelastic membranes for large deformation, fracture, and out-plane tearing.

## CRediT authorship contribution statement

**Yang Yang:** Writing – review & editing, Writing – original draft, Supervision, Methodology, Conceptualization. **Yujie Chen:** Writing – original draft, Software, Data curation. **Yijun Liu:** Writing – review & editing, Supervision.

## Declaration of competing interest

The authors declare that they have no known competing financial interests or personal relationships that could have appeared to influence the work reported in this paper.

## Data availability

Data will be made available on request.

## Acknowledgments

The authors would like to thank the financial support from National Natural Science Foundation of China (Project Nos. 12272160 and 12372198) and the Shenzhen National Science Foundation (Project No. 20231129213819001).

## References

- [1] Silling SA. Reformulation of elasticity theory for discontinuities and long-range forces. *J Mech Phys Solids* 2000;48:175–209.
- [2] Roy P, Behera D, Madenci E. Peridynamic simulation of finite elastic deformation and rupture in polymers. *Engng Fract Mech* 2020;236:107226.
- [3] Chen YJ, Yang Y, Liu YJ. Large deformation and crack propagation analyses of hydrogel by peridynamics. *Engng Fract Mech* 2023;248:109261.
- [4] Chen YJ, Yang Y, Liu YJ. Fatigue crack growth analysis of hydrogel by using peridynamics. *Int J Fract* 2023.
- [5] Silling SA, Bobaru F. Peridynamic modeling of membranes and fibers. *Int J Non Linear Mech* 2005;40:395–409.
- [6] Bang DJ, Madenci E. Peridynamic Modeling of Hyperelastic Membrane Deformation. *J Engng Mater Technol* 2017;139:031007.
- [7] Li H, Zheng YG, Zhang YX, et al. Large deformation and wrinkling analyses of bimodular structures and membranes based on a peridynamic computational framework. *Acta Mech Sin* 2019;35(6):1226–40.
- [8] Oterkus E, Madenci E, Oterkus S. Peridynamic shell membrane formulation. *Procedia Struct Integrity* 2020;28:411–7.
- [9] Ozdemir M, Oterkus S, Oterkus E, et al. Fracture simulation of viscoelastic membranes by ordinary state-based peridynamics. *Procedia Struct Integrity* 2022;41:333–42.
- [10] Yang ZH, Ma CC, Oterkus E, Oterkus S, et al. Analytical solution of the peridynamic equation of motion for a 2-dimensional rectangular membrane. *Journal of peridynamics and nonlocal modeling* 2023;5:375–91.
- [11] Madenci E, Oterkus E. *Peridynamics theory and its applications*. Springer; 2014.
- [12] Liu YX, Liu LS, Mei H, et al. A modified rate-dependent peridynamic model with rotation effect for dynamic mechanical behavior of ceramic materials. *Computer Method in Applied Mechanics and Engineering* 2022;388:114246.
- [13] Le QV, Chan WK, Schwartz J. A two-dimensional ordinary, state-based peridynamic model for linearly elastic solids. *International Journal for Numerical Method in Engineering* 2014;98:547–61.
- [14] Yang S, Gu X, Zhang Q, et al. Bond-associated non-ordinary state-based peridynamic model for multiple spalling simulation of concrete. *Acta Mech Sin* 2021:1–32.
- [15] Song Y, Yu H, Kang Z. Numerical study on ice fragmentation by impact based on non-ordinary state-based peridynamics. *Journal of Micromechanics and Molecular Physics* 2019;4:1850006.
- [16] Silling SA, Epton M, Weckner O, Xu JF, Askari E. Peridynamic States and Constitutive Modeling. *J Elast* 2007;88:151–84.
- [17] Breitenfeld MS, Geubelle PH, Weckner O, Silling SA. Non-ordinary state-based peridynamic analysis of stationary crack problems. *Comput Methods Appl Mech Engng* 2014;272:233–50.
- [18] Yaghoobi A, Chorzepa MG. Higher-order approximation to suppress the zero-energy mode in non-ordinary state-based peridynamics. *Comput Struct* 2017;188:63–79.
- [19] Chen HL, Spencer BW. Peridynamic bond-associated correspondence model: Stability and convergence properties. *Int J Numer Meth Engng* 2018;117(6):713–27.
- [20] Chen HL. Bond-associated deformation gradients for peridynamic correspondence model. *Mech Res Commun* 2018;90:34–41.

- [21] Gu X, Zhang Q, Madenci E, Xia X. Possible causes of numerical oscillations in non-ordinary state-based peridynamics and a bond-associated higher-order stabilized model. *Comput Methods Appl Mech Engng* 2019;357:112592.1–112592.36.
- [22] Behera D, Roy P, Madenci E. Peridynamic correspondence model for finite elastic deformation and rupture in Neo-Hookean materials. *Int J Non Linear Mech* 2020;126:103564.
- [23] Zaccariotto M, Mudric T, Tomasi D, Shojaei A, Galvanetto U. Coupling of FEM meshes with Peridynamic grids. *Computer Method in Applied Mechanics and Engineering* 2018;330:471–97.
- [24] Madenci E, Dorduncu M, Barut A, Phan N. A state-based peridynamic analysis in a finite element framework 2018;195:104–28.
- [25] Yang Y, Liu YJ. Modeling of cracks in two-dimensional elastic bodies by coupling the boundary element method with peridynamics. *International Journal of Solids Structures* 2021;217–218:74–89.
- [26] Yang Y, Liu YJ. Analysis of dynamic crack propagation in two-dimensional elastic bodies by coupling the boundary element method and the bond-based peridynamics. *Computer Method in Applied Mechanics and Engineering* 2022;399:115339.
- [27] Bergel GL, Li S. The total and updated lagrangian formulations of state-based peridynamics. *Comput Mech* 2016;58(2):351–70.
- [28] Yan J, Li S, Zhang AM, et al. Updated lagrangian particle hydrodynamics (ULPH) modeling and simulation of multiphase flows. *J Comput Phys* 2019;393:406–37.
- [29] Zhang Q, Li SF, Zhang AM, et al. A peridynamic Reissner-Mindlin shell theory. *Int J Numer Meth Engng* 2020;122:122–47.
- [30] Gu X, Zhang Q, Madenci E, Xia X. Possible causes of numerical oscillations in non-ordinary state-based peridynamics and a bond-associated higher-order stabilized model. *Computer Method. Appl Mech Engng* 2019;357:112592.1–112592.36.
- [31] Hu Y, Chen HL, Spencer BW, Madenci E. Thermomechanical peridynamic analysis with irregular non-uniform domain discretization. *Engng Fract Mech* 2018;197:92–113.
- [32] Ayatollahi MR, Mahdi HM, Dehghany M, Berto F. A new criterion for rupture assessment of rubber-like materials under mode-I crack loading: the effective stretch criterion. *Adv Engng Mater* 2016;18(8):1364–70.